



Available online at www.sciencedirect.com



CrossMark

ScienceDirect

Proceedings of the Combustion Institute 37 (2019) 943–951

Proceedings
of the
Combustion
Institute

www.elsevier.com/locate/proci

Flame temperature effect on sp^2 bonds on nascent carbon nanoparticles formed in premixed flames ($T_{f,max} > 2100$ K): A Raman spectroscopy and particle mobility sizing study

Jonathan Bonpua, Yuniba Yagües, Aleksandr Aleshin, Shruthi Dasappa,
Joaquin Camacho*

Mechanical Engineering Department, San Diego State University, San Diego, CA 92182, USA

Received 1 December 2017; accepted 15 June 2018

Available online 1 September 2018

Abstract

The evolution in carbon particle size and carbon bonds was observed with increasing flame temperature for a fixed growth time ($t_p \sim 13$ ms) and equivalence ratio ($\Phi = 2.5$) in set of sooting premixed stagnation flames. For carbon formed in each flame, detailed particle size distribution functions (PSDF) and Raman spectra (excitation energy of 2.33 eV) were measured as the maximum flame temperature increased from $1911\text{ K} < T_{f,max} < 2263\text{ K}$. The PSDF steadily decreased in size and narrowed in width as the flame temperature increased, a trend which reversibility in precursors is expected to cause for carbon particles formed at elevated temperatures. Several features of the Raman spectra were used to analyze carbon bonds on the flame-formed carbon with increasing flame temperature. Typical features of Raman spectra corresponding to soot were observed for carbon products formed with $T_{f,max} = 1911$ K. The widths of the overall G (sp^2 in ideal graphite) and D (sp^2 defects) Raman bands narrowed significantly in spectra from elevated temperature flame carbon. The intensity of the amorphous band (D3) relative the G band decreased. For carbon products of the lower temperature flames, a relatively wide band in the vicinity of 1600 cm^{-1} encompassing the G band was observed. As the flame temperature increased, two separate peaks were observed in this region; the G band and a separate band in the vicinity of 1620 cm^{-1} . The characteristic distance between defects was estimated to grow from 1 nm to 2 nm for carbon products formed at $T_{f,max} = 1911$ K and 2260 K, respectively. The corresponding surface area observed at these conditions was on the order of 600 nm^2 and 200 nm^2 per particle, respectively, which indicates the relative area of ordered structures on the particle increases.

© 2018 The Combustion Institute. Published by Elsevier Inc. All rights reserved.

Keywords: Soot; Carbon; Nanoparticle; Mobility sizing; Raman spectroscopy; Graphitization

* Corresponding author.

E-mail address: jcamacho@sdsu.edu (J. Camacho).

1. Introduction

The structure of soot and flame-formed carbon contains amorphous and graphitic components with wide variations depending on many of factors [1–4]. The structure details depend on properties of the growth environment such as fuel structure [2], growth time/particle age [5–9], temperature [10] and gas-phase composition [6,11–14]. This leads to a wide range of known structures for carbon particulate products emanating from flames and combustion-powered devices (see e.g [15]). The variety in structures introduces environmental [16] and health ramifications [17] for combustion-based emissions. In addition, the diversity in flame-produced carbon has enabled selective production of functional carbon nanomaterials [18–21].

As first demonstrated fully in Sadezky et al. [22], the Raman spectra of soot and related carbon materials can be used to elucidate fine structural details. Analysis of Raman spectra has greatly contributed to the refinement of soot parameters such as the absorption cross-section (see e.g. [23]), optical bandgap (see e.g [24]) and graphitic crystallite size (see e.g [25]). Investigations of soot formed in engines exist [15,22] but more systematic observations in terms of fundamental formation and growth factors have been carried out in laboratory flames. The Raman spectra of flame-formed carbon has been analyzed in laminar premixed flames [7,8,13,26,27], co-flow diffusion flames [9,25,28,29], inverted diffusion flames [23] and inverse flames [24]. In the current work, the evolution in nascent flame-formed carbon nanoparticle structure will be investigated by systematically observing the effect of flame temperature in a set of pseudo one-dimensional premixed flames. Specifically, the evolution of Raman spectra for carbon products formed in separate flames under similar growth times will be examined in premixed flat flames having temperatures spanning 1900–2260 K.

The unique stabilization mechanism of premixed flat flames (also known as stretch-stabilized flames and stagnation flames) does not rely on heat loss to the burner and this enables relatively high flame temperatures to be accessed [30]. The high temperatures are expected to allow for observation of carbon nanoparticles having C/H ratios greater than commonly reported for flame soot. Dehydrogenation from the particle surface is expected at higher temperatures based on the thermodynamic prediction that hydrogen gas evolution drives the process due to entropy increase [4]. Starting from the extensive work of Dobbins and co-workers [5,10,31], the kinetics of soot particle carbonization have also been developed to describe the evolution from precursor particles to particles having decreased hydrocarbon-to-carbon ratio [32–36]. Details of the Raman spectra will be assessed in the current study to describe the nature

of carbon bonds for particles formed in flames with elevated flame temperatures.

The evolution of particle size distribution function (PSDF) will also be measured by mobility sizing to give further details on the nascent carbon nanoparticle structure. Extensive studies on the evolution of nascent soot PSDF exist in terms of flame temperature [37–39], fuel structure [40–46], sooting level/equivalence ratio [39,47,48] and age [7,49] but systematic measurements of PSDFs from relatively high-temperature ($T_{f,max} > 2100$ K) flames have only been recently been achieved with the introduction of probed premixed flat flames [50]. In addition, embedding a probe at the stagnation surface enables probe sampling and sample deposition with boundary conditions more precisely defined than other probe and deposition geometries [51–53]. The combination of Raman spectroscopy and mobility sizing has been carried out in several works [8,13,18,23] but a unique focus of the current work is the flame temperature effect at relatively high temperature (1900 K $< T_{f,max} <$ 2260 K) for flame-formed carbon nanoparticles in the nucleation and early growth stages.

2. Experimental

The experiments center around the stationary premixed planar flame in stagnation flow [30] which is stabilized by flow-stretch rather than heat loss. In these flames, temperatures can approach or exceed the adiabatic flame temperature depending on the Lewis number [30]. In the current work, the flow stagnation is induced by a solid aluminum plate with a sampling probe orifice embedded flush to the stagnation surface. The experimental setup, summarized in Fig. 1, includes an aerodynamically shaped nozzle (nozzle diameter is 1.43 cm), a stagnation surface/sampling probe assembly and a Scanning Mobility Particle Sizer (SMPS) setup. The nozzle, sampling assembly and sampling procedures have been discussed previously [50–52]. The SMPS setup, however, has changed significantly. The TSI 1 nm Scanning Mobility Particle Sizer is used here (TSI 3838E77). This system is composed of a dual voltage classifier (TSI 308,202), a Kr-85 bi-polar diffusion charger (Neutralizer TSI 3077A), 1 nm differential mobility analyzer (DMA) (TSI 3086), a diethylene glycol-based (DEG) condensation particle counter (CPC) (so-called Nanoenhancer, TSI 3777) and a butanol-based CPC (TSI 3772). TSI Aerosol Instrument Manager Software (version 10.2) is used to collect and export the PSDFs.

The DEG-based CPC is meant to allow for counting of particles with mobility diameters as small as 1.4 nm. Mobility sizing of soot in the DMA can classify particles approaching 1 nm but counting particles in this size range has required faraday cup electrometers [54,55] or, more recently,

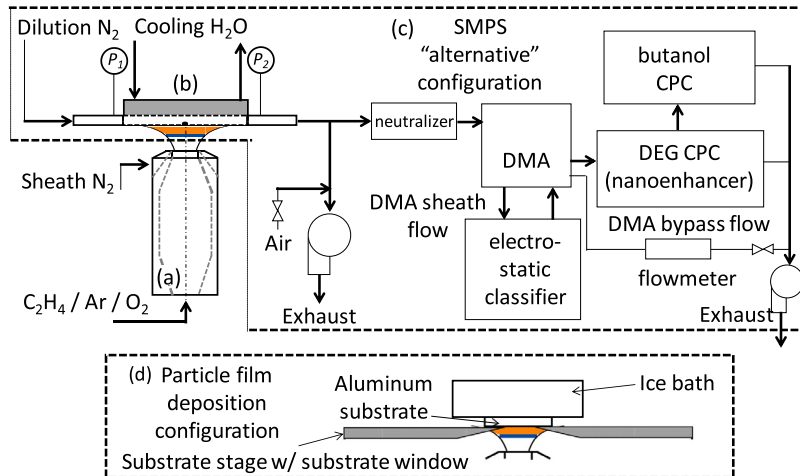


Fig. 1. Experimental setup consisting of an aerodynamically shaped nozzle (a), a stagnation surface/sampling probe assembly (b) an SMPS in the “alternative” configuration defined by the vendor (c), and the setup for collecting flame formed carbon deposits for off-line analysis (d).

Table 1

Flame parameters^a and lognormal distribution parameters measured for the large particle-size mode^f.

C ₂ H ₄ ^b	O ₂ ^b	Ar ^b	T _{f,max} ^c (K)	t _p (L) ^d (ms)	Velocity ^e , v _o (cm/s)	Separation distance, L (cm)	N ₂ × 10 ⁻¹⁰ (cm ⁻³) ^f	σ _{g,2} ^f	$\langle D_{m,2} \rangle^f$ (nm)
0.131	0.158	0.711	1911	14	46.5	1.4	—	—	—
0.145	0.173	0.682	1987	13	53.1	1.4	4.9	2.0	13.0
0.150	0.180	0.670	2030	13	51.2	1.4	—	—	—
0.160	0.192	0.648	2083	13	47.9	1.4	8.9	1.6	8.5
0.175	0.210	0.615	2164	14	101.1	2.5	9.0	1.4	6.8
0.183	0.220	0.597	2221	13	96.6	2.5	8.5	1.4	7.2
0.196	0.236	0.569	2255	6	106.8	2.5	7.0	1.3	6.1
0.196	0.236	0.569	2260	13	88.0	1.4	5.3	1.3	7.6
0.196	0.236	0.569	2263	16	84.8	3.6	4.6	1.4	8.4

^a All unburned mixtures have the equivalence ratio equal to 2.5.

^b Mole fractions.

^c Computed using OPPDIF and USC Mech II with T_{burner} = 343 K and T_{probe} = 410 K.

^d Computed based on the time to reach the position of T_{f,max} to the position of the stagnation surface.

^e Unburned gas velocity at 298 K and 1 atm. Sheath N₂ velocity for each flame is v_o.

^f The 2 subscript denotes the lognormal distribution parameters of the larger growth mode.

DEG-based CPCs [49]. As Fig. 1 shows, the SMPS is in the “alternative” configuration suggested by TSI to minimize diffusion losses before the CPCs. The flow into the neutralizer is 5 SLPM and 2.5 SLPM flows into the DMA, the balance of which bypasses to exhaust. The sheath flow through the DMA (25 SLPM) is controlled in the electrostatic classifier housing and this gives a 10:1 sheath to aerosol flow. The DMA polarity is set to positive in the current work. The mobility diameter is corrected here for free molecular regime effects [56].

The series of flames, all premixed ethylene–oxygen–argon flames, are designed to isolate the temperature effect on evolution of carbon structure and particle size. The flame flow parameters and corresponding PDSF parameters measured for each flame are summarized in Table 1. The flame

structure was predicted by OPPDIF calculations [57,58] using USC Mech II [59] with multicomponent transport, thermal diffusion and radiation of CO₂ and H₂O considered. As discussed previously, reasonable agreement between the OPPDIF prediction and measured flame position can be achieved if plug flow exists at the burner boundary and the nozzle-to-separation distance ratio is below unity [50]. The maximum flame temperature, T_{f,max}, is largely dependent upon the flame diluent (argon) in stagnation flat flames and the flame diluent mole fraction was adjusted to give 1911 K < T_{f,max} < 2263 K all at Φ = 2.5.

The flame standoff distance (considered here to be the position of maximum flame temperature to position of the stagnation surface) is determined by the kinematic balance between the

local flame speed and the normal flow velocity immediately upstream of the flame surface [30]. For a given flame temperature, the flame standoff distance was manipulated by a combination of cold flow velocity and nozzle-to-stagnation surface separation distance, L , manipulation. In the current work, these combinations were designed to achieve similar growth times (~ 13 ms) for the seven flame temperature conditions studied. The growth time, t_p , listed in Table 1 is considered to be the time to traverse through the flame standoff distance at the convective and thermophoretic velocity predicted by OPPDIF [50]. A set of experiments with varying growth time was also carried out for the highest temperature flame. As will be discussed below, the PSDF was fitted to a lognormal distribution for the larger growth mode (subscript 2 in Table 1). In addition, the PSDF were not measured for $T_{f,max} = 1911$ and 2030 K because the PSDF is expected to resemble the measurements taken at nearby temperature conditions.

The maximum flame temperature was measured for the hottest temperature flame by analyzing images taken by a commercial DSLR camera (NIKON D3400) with the infrared filter removed. Three separate images were recorded with different bandpass filters (450 nm, 650 nm and 900 nm, Andover FS20) placed in front of the camera lens. A two-color carbon pyrometry technique [57] was applied assuming that each filtered image corresponds to “color” specific intensity of blackbody radiation emanating from the flame carbon. Further details on the temperature measurement are in the supplementary material. The OPPDIF prediction for the hottest flame at $t_p = 13$ ms is $T_{f,max} = 2260$ K. The result of the pyrometry measurement at this condition was $T_{f,max} = 2250 \pm 55$ K where this reported value is the midpoint of a 110 K range of predictions resulting from 15 combinations of filter intensity ratios and camera shutter speeds.

Raman spectroscopy was carried out off-line for carbon deposits collected from each flame studied. The sampling probe/stagnation probe assembly was removed and replaced with a separate stagnation surface, shown in Fig. 1, designed to serve as a stage for deposition substrates over the flame. The stage is a 2 mm thick aluminum, water-cooled stagnation surface that was designed with a 3 cm diameter window to mount 1 mm thick aluminum plates (3 cm × 3 cm) over the area of the flat flame. The window was tapered such that deposition plates were effectively flush giving a nozzle-to-stagnation separation distance identical to the corresponding probe sampling experiments. Aluminum was chosen over quartz as the deposition surface material because high thermal conductivity is required to maintain the 400 K temperature at the deposition surface. The heat flux emanating from the hottest flames induces excessive temperatures at the deposition surface which causes a significant loss in deposition efficiency if cooling heat transfer is not

fast enough. An ice bath in a thin-walled SS vessel placed over the aluminum deposition surface was necessary to enable deposition of flame particles with a steady boundary condition. The temperature of the deposition surface was monitored by a thin wire (0.125 micron) type K thermocouple placed on the non-deposition side of the aluminum plate and under the ice bath. The deposition temperature was maintained at 430 ± 20 K for all flame conditions. A Thermo DXR2 Raman Microscope with a 532 nm excitation source was used to measure Raman spectra with Raman shifts spanning 300–3000 cm^{-1} . The laser was focused under a 50x objective at 1 mW power and care was taken to prevent modifications to the carbon structure by laser excitation. A temporary fluorescence background was observed (which is evidence that adsorbed gas-phase PAH is not present in the samples) but spectra were only analyzed after the background intensity reached a steady level.

3. Results and discussion

The premixed flat flames studied herein have a pseudo one-dimensional flame structure [58] that can be manipulated to systematically observe carbon-formation in terms of growth time and temperature. The current series of flames are designed to isolate the effect of flame temperature for a fixed growth time ($t_p \sim 13$ ms) and equivalence ratio ($\Phi = 2.5$). As Table 1 shows, this was achieved for each flame by a suitable combination of argon flame diluent concentration, total flow velocity and nozzle-to-stagnation separation distance. The evolution of mobility diameter PSDF from $1987 \text{ K} < T_{f,max} < 2260 \text{ K}$ with a fixed growth time with $t_p \sim 13$ ms is shown in Fig. 2. The qualitative features of the current PSDFs are similar to those previously reported in lightly sooting premixed flames approaching 2000 K flame temperatures [37,39,44,45]. Namely, the size of particles decreases as the temperature increases for a given equivalence ratio.

Analysis of the quantitative features of so-called nucleation mode of particles below 2 nm is limited by experimental uncertainties. Specifically, systematic work by Carbone and co-workers [54,55] has shown that the typical bi-polar diffusion chargers can deviate from the assumed charge distribution (in terms of number and +/- symmetry) depending on the time duration of diffusion charging, particle size, particle composition and amount of pre-ionized particles. Another limitation of the current nucleation mode measurement is the unknown penetration of small particles through the SMPS in the “alternative” configuration. Even though the penetration is not known, this configuration is recommended by TSI because the particle loss due to diffusion in the conventional configuration is excessively higher. Solutions

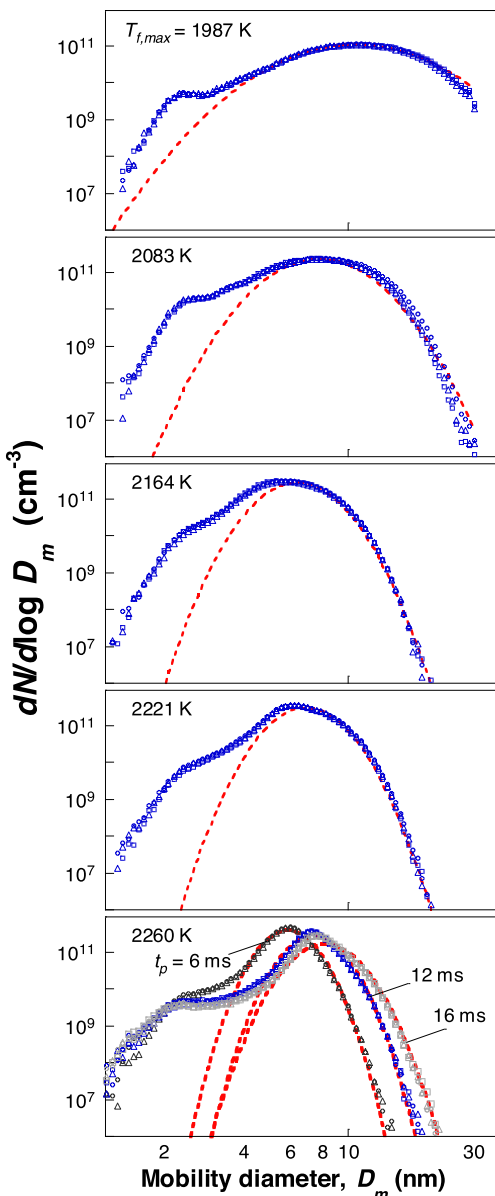


Fig. 2. Measured PSDFs for flame-formed carbon with growth time and equivalence ratio fixed at $t_p \sim 13$ ms and $\Phi = 2.5$. Symbols are 3 separate experimental runs and the dotted line is a fit to the log-normal distribution for the growth mode of the PDSF. The particle growth time was varied in the case of $T_{f,max} = 2260$ K (bottom row).

to the aforementioned challenges are beyond the scope of the present study. Measured PSDFs are presented here with observed nucleation modes suffering from uncertainty but not artificially altered by the diffusion correction option in the AIM software. The penetration of nucleation size particles is

less than 5% even without the additional equivalent length introduced by the DEG-CPC pathway.

The larger-size growth mode is the focus of the current analysis and fits to a log-normal distribution are shown in Fig. 2 with parameters tabulated in Table 1. The evolution begins at $T_{f,max} = 1987$ K with a growth mode centered at $(D_{m,2}) = 13.0$ nm. As expected, the median particle size decreases as the temperature is increased under comparable conditions. A corresponding narrowing of the distributions is also observed. For the first time, PSDFs were measured from premixed flames having temperatures exceeding 2200 K. The relatively high $\Phi = 2.5$ was chosen because the PSDF was expected to decrease substantially due to reversibility in soot precursor growth [4,33,50] at elevated temperatures. The PDSFs in flames exceeding 2200 K in temperature show somewhat of a split between the nucleation and growth modes over time. This split is exemplified in measured PSDFs shown in Fig. 4 with $T_{f,max} = 2260$ K for a series of $t_p = 6, 12$ and 16 ms. These measured PSDF show a nucleation mode at the earliest growth stage that stays relatively static as the growth mode increases to larger sizes over time.

Raman spectra were measured for each flame to observe the evolution in carbon structure with flame temperature. The well-defined boundary condition of sampling at a stagnation surface that has served as a useful compliment to soot modeling studies (see e.g., [35,44,60–63]) is extended in the current work for deposition of nanoparticle films. Raman spectra measured off-line correspond to the same condition that the PSDF were measured and any discrepancy in the material properties, i.e. PSDF and sp^2 bonding, between aerosol and deposited samples is expected to be insignificant. The temperature throughout the thin deposited carbon layer is expected to be uniformly low which would indicate that temperature induced modifications over time are minimal. The evolution in first-order ($1000–1780\text{ cm}^{-1}$) Raman spectra of as-deposited carbon with respect to flame temperature for a fixed particle growth time and equivalence ratio ($t_p \sim 13$ ms and $\Phi = 2.5$) is shown in Fig. 3. The measured spectra before baseline correction including the secondary bands ($100–3500\text{ cm}^{-1}$) are in the supplemental material. Spectrum intensities were normalized to the highest intensity value measured in the spectrum and a polynomial was used in Matlab to correct the luminescent background. Details on the baseline correction and insensitivity to the polynomial order is included in the supplemental material. Striking trends and fine details about the evolution in carbon bonds can be elucidated for the $1911\text{ K} < T_{f,max} < 2263\text{ K}$ series presented in Fig. 3. The expected first-order G and D bands relating to sp^2 carbon networks are observed in products of each flame but major differences in details in these bands are observed. A 5-band curve-fitting technique was applied in Matlab following the

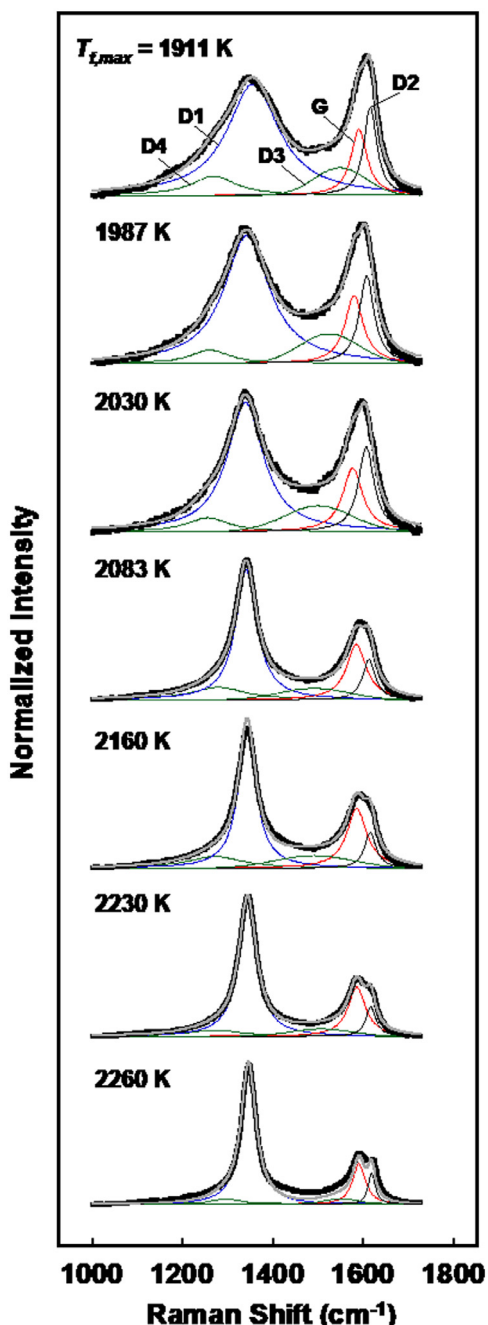


Fig. 3. Measured Raman spectra for flame-formed carbon with growth time and equivalence ratio fixed at $t_p \sim 13$ ms and $\Phi = 2.5$. The bold black line is the measured spectra and the grey line is the curve fit composed of 5 different bands. The deconvoluted bands curve fits are also shown.

methods and band designations of Sadezky et al. [15,22]. Following the methods of Tuinstra and Koenig [64] and others since, the details of the G and D bands of the Raman spectrum will be assessed [64–66]. The D2 band has been proposed to originate from surface graphene defects [66], the D3 band has been attributed to amorphous carbon, and the D4 band has been attributed to polyenes and/or ionic impurities [22]. All of the above-mentioned bands were fitted with Lorentzian shapes except for the D3 band (Gaussian).

Typical features of Raman spectra corresponding to soot were observed for carbon products formed with $T_{f,max} = 1911$ K. The widths of the overall G and D bands narrowed significantly in spectra corresponding to flame carbon formed at elevated temperature. For carbon products of the lower temperature flames, a relatively wide band in the vicinity of 1600 cm^{-1} encompassing the G band was observed in the Raman spectra. As the flame temperature increased, two separate peaks were observed in this region; the G band and a separate band in the vicinity of 1620 cm^{-1} . Recent theoretical predictions of Raman spectra for carbon materials having relatively small graphite-like regions rule out the proposed double resonance origin of the D2 band [69]. However, discussion of the D2 band origin is beyond the scope of this work and band in the vicinity of 1620 cm^{-1} will be denoted as D2 for illustrative purposes.

The intensity ratio of the D1 peak relative to G gives insight into the evolution of carbon structure for particles formed at increasing flame temperature. The amorphous band (D3) intensity relative the G band decreases for particles formed at elevated flame temperature. Both of these trends have been shown to indicate increasing structural order which implies that the particles formed under increasing flame temperatures have a relatively ordered structure [22,67,68]. A dramatic evolution of the D2 band intensity relative the G band occurs. For Raman spectra corresponding to carbon formed at lower temperature, the D2 intensity is greater than the G band intensity. For particles formed at higher temperatures, then the relative intensity flips such that the G band intensity is higher than the D2 band. Similar prominent D2 features were discussed in reference to graphite lattice order in flame-formed nano-disks [18] but the relative intensity and sharpness of the D2 are unique to the current work. A series Raman spectra corresponding to flame-formed carbon samples formed in flames with $T_{f,max} = 2260$ K and $t_p = 6, 13$ and 16 ms is shown in Fig. 4. The prominent and relatively isolated D2 peaks are also observed for earlier and later times at $T_{f,max} = 2260$ K.

The ratio of D and G band intensities are regularly used to quantify structural parameters such as the in-plane crystallite size, the characteristic distance between defects and graphitic crystallite aspect ratios. The intensity of the G band, I_G , is

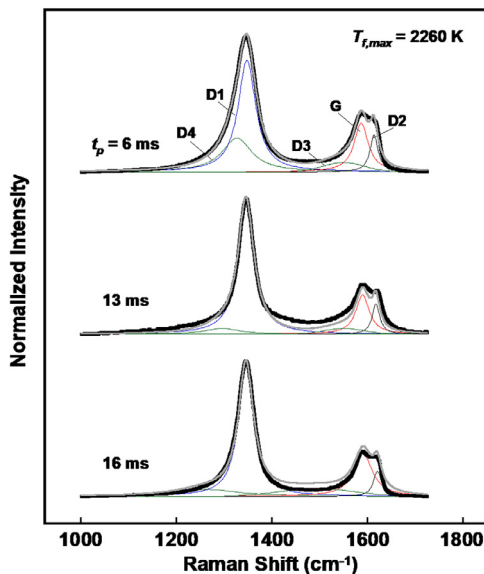


Fig. 4. Measured Raman spectra for flame-formed carbon with $T_{f,\max} = 2260$ K and $\Phi = 2.5$.

known to be proportional to the sample area and the intensity of the D1 band, I_D , is known to scale with edge of defects in the lattice [68]. Due to the expected amorphous structure for products of low temperature flames, the intensity of the two bands will be correlated to the characteristic distance between defects, L_d , in the high defect density regime [68]:

$$L_d^2 = 5.4 \times 10^{-2} E_L^4 \frac{I_D}{I_G}$$

where L_d is in nanometers and the Raman excitation energy, E_L is inputted in eV (2.33 eV currently). Intensity ratios with respect to the G band are shown in Fig. 5. The ratio I_{D1} / I_G and I_{D2} / I_G consider the deconvoluted peak intensities of D1, D2 and G. I_{D2}/I_{D1} is also shown. The prediction of the distance between defects based on the above equation is also included in Fig. 5. The distance between defects, L_d , increases from 1.6 nm for carbon formed with $T_{f,\max} = 1911$ K to 2.3 nm for carbon formed with $T_{f,\max} = 2260$ K. The defect distance at $T_{f,\max} = 1911$ K is slightly higher than the in-plane graphite crystallite size reported for soot and related carbon materials. The sharpest change in intensity ratios is observed between carbon products formed in flames having $T_{f,\max} = 2030$ and 2083 K and a flip in the intensity ratio between D2 and G is observed here as well. The systematic transition from ordered graphene layers to carbon with a high defect density has been previously described [68] in terms of bands and intensity ratios of the Raman spectra. The narrowing of the Raman bands and increasing I_{D1}/I_G ratio with in-

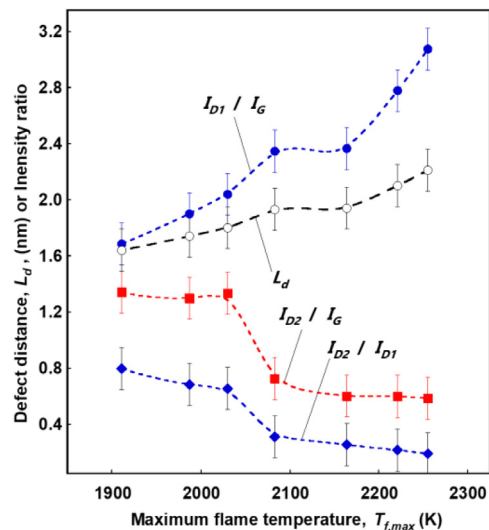


Fig. 5. Intensity ratios and characteristic distance between defects, L_d , for the series of flames studied. Lines are drawn to guide the eye.

creasing flame temperature currently observed indicates that flame formed carbon follows this trend in reverse. Namely, the global structure of flame formed carbon transitions from high defect density carbon at lower temperature to more ordered layers at higher flame temperature. The overall trend in crystallite growth observed currently agrees with reports on aromatic sp^2 on soot with growing mass and age [8,23–29] but the current observations give further details on the evolution as a function of flame temperature.

The evolution in PSDF and Raman spectra for flame-formed carbon as a function of flame temperature presented here sheds light on evolution of aromatic sp^2 bonds and other details of structural order during early growth stages. Firstly, the range of PSDF observed confirms that the evolution in Raman spectra is observed for flame carbon in early growth stages. A rough estimate of the surface area per particle is on the order of 500 and 200 nm² for particles formed at $T_{f,\max} = 1911$ and 2260 K, respectively. This estimate is based on the median diameter of growth mode listed in Table 1. While the surface area (size) per particle decreases with temperature, the characteristic length between defects increases. This implies that the relative fraction of aromatic sp^2 area (or order) on the particle surface increases with flame temperature for the conditions studied. The effect on surface curvature is also expected to affect the interpretation of the Raman spectra in terms of carbon structure, especially for relatively small particles.

For a distribution of particle sizes, the variation in particle structure will naturally increase but any observed effect on the local carbon structure

giving rise to the Raman spectra is difficult to discern. Narrowing of bandwidths has been explained on a sound basis of graphitization and structure disorder but this effect has only been considered for monodisperse size (particle or grain) distribution. The ability to observe PSDF with varied geometric standard deviations also allows for the exploration of the size distribution effect on Raman spectra. More information on details of the global particle structure beyond insights into sp^2 bonding are needed. Future work including microscopy and other analyses will further elucidate the flame temperature effect on the evolution in flame-formed carbon particle size and graphite-like structure.

4. Conclusion

The evolution in PSDF and Raman spectra corresponding to carbon particles formed in premixed flames with increasing flame temperature was observed. The measurements were taken for a fixed growth time ($t_p \sim 13$ ms) and equivalence ratio ($\Phi = 2.5$). Details of the flame-formed carbon structures were elucidated from these evolutions spanning $1911\text{ K} < T_{f,max} < 2263\text{ K}$. The PSDF began with a growth mode centered at $\langle D_{m,2} \rangle = 13.0\text{ nm}$ for $T_{f,max} = 1987\text{ K}$ and steadily decreased in size as the flame temperature increased, a trend which reversibility in precursors is expected to cause at these elevated temperatures. For the first time, the detailed PSDF of carbon formed in flames having $T_{f,max} > 2200\text{ K}$ is presented here. For these PSDF, a bimodal distribution is observed and the evolution with time leads to an increase in the growth mode from $\langle D_{m,2} \rangle = 6.1\text{--}8.4\text{ nm}$ while the nucleation mode stays static in terms of size and number.

Information about the evolution in carbon structure was also observed by Raman spectroscopy analysis. Several features of Raman spectra measured from flame-formed carbon were used to analyze the evolution in sp^2 carbon bonding and structure ordering with increasing flame temperature. The bandwidths of the overall G and D bands narrowed significantly in Raman spectra of particles formed at elevated temperature. The intensity of the amorphous band (D3) and defect (D2) band relative the G band decreased as well. A unique feature of the Raman spectra observed here was the prominence of D2 band in terms of the dramatic evolution with flame temperature and eventual bandwidth narrowing leading to a distinct peak emerging. The intensity ratios of the D1 and D2 peaks relative to G gave insight into the carbon structure as a function of flame temperature. These ratios allowed for the prediction of the distance between defects increasing from 1 nm to 2 nm for particles formed under increasing temperature while the corresponding particle size dropped. The measurements obtained here un-

der well-defined boundary conditions are expected to compliment theoretical and modeling studies of size and carbon structure evolution in flames.

5. Acknowledgments

The work was supported the San Diego State University Grants Program. The authors are thankful to Prof. David Pullman (SDSU) for assistance and helpful discussions concerning Raman Spectroscopy and Jeremy Brunenmeyer for assistance with sample collection. Sean Richards was also very helpful during the experimental setup.

Supplementary materials

Supplementary material associated with this article can be found, in the online version, at doi:[10.1016/j.proci.2018.06.124](https://doi.org/10.1016/j.proci.2018.06.124).

References

- [1] H. Bockhorn, *Soot Formation in Combustion*, Springer-Verlag, Berlin, 1994.
- [2] R.L. Vander Wal, A.J. Tomasek, *Combust. Flame* 136 (2004) 129–140.
- [3] A. D’Anna, *Proc. Combust. Inst.* 32 (2009) 593–613.
- [4] H. Wang, *Proc. Combust. Inst.* 33 (2011) 41–67.
- [5] R.A. Dobbins, R.A. Fletcher, H.C. Chang, *Combust. Flame* 115 (1998) 285–298.
- [6] M. Alfè, B. Apicella, R. Barbella, J.N. Rouzaud, A. Tregrossi, A. Ciajolo, *Proc. Combust. Inst.* 32 (2009) 697–704.
- [7] M. Commodo, G. Tessitore, G. De Falco, A. Bruno, P. Minutolo, A. D’Anna, *Proc. Combust. Inst.* 35 (2015) 1795–1802.
- [8] M. Commodo, G. De Falco, A. Bruno, C. Borriello, P. Minutolo, A. D’Anna, *Combust. Flame* 162 (2015) 3854–3863.
- [9] M. Commodo, P.H. Joo, G. De Falco, P. Minutolo, A. D’Anna, Ö.L. Gülder, *Energy Fuels* 31 (2017) 10158–10164.
- [10] R.A. Dobbins, *Combust. Flame* 130 (2002) 204–214.
- [11] C. Russo, M. Alfè, J.-N. Rouzaud, F. Stanzione, A. Tregrossi, A. Ciajolo, *Proc. Combust. Inst.* 34 (2013) 1885–1892.
- [12] B. Apicella, P. Pré, M. Alfè, A. Ciajolo, V. Gargiulo, C. Russo, A. Tregrossi, D. Deldique, J.N. Rouzaud, *Proc. Combust. Inst.* 35 (2015) 1895–1902.
- [13] M. Sirignano, A. Ciajolo, A. D’Anna, C. Russo, *Energy Fuels* 31 (2017) 2370–2377.
- [14] C.-H. Huang, R.L. Vander Wal, *Combust. Flame* 168 (2016) 403–408.
- [15] M. Saffarpour, L.-L. Tay, K.A. Thomson, et al., *Aerosol Sci. Technol.* 51 (2017) 518–531.
- [16] R.J. Charlson, S.E. Schwartz, J.M. Hales, R.D. Cess, J.A. Coakley, J.E. Hansen, D.J. Hoffmann, *Science* 255 (1992) 423–430.
- [17] I.M. Kennedy, *Proc. Combust. Inst.* 31 (2007) 2757–2770.
- [18] P. Minutolo, M. Commodo, A. Santamaria, G. De Falco, A. D’Anna, *Carbon* 68 (2014) 138–148.

- [19] M.J. Height, J.B. Howard, J.W. Tester, J.B. Vander Sande, *Carbon* 42 (2004) 2295–2307.
- [20] S. Li, Y. Ren, P. Biswas, S.D. Tse, *Prog. Energy Combust. Sci.* 55 (2016) 1–59.
- [21] N.K. Memon, S.D. Tse, J.F. Al-Sharab, et al., *Carbon* 49 (2011) 5064–5070.
- [22] A. Sadezky, H. Muckenhuber, H. Grothe, R. Niessner, U. Poschl, *Carbon* 43 (2005) 1731–1742.
- [23] R. Dastanpour, A. Momenimovahed, K. Thomson, J. Olfert, S. Rogak, *Carbon* 124 (2017) 201–211.
- [24] C. Russo, B. Apicella, J.S. Lighty, A. Ciajolo, A. Tregrossi, *Carbon* 124 (2017) 372–379.
- [25] J.D. Herdman, B.C. Connolly, M.D. Smooke, M.B. Long, J.H. Miller, *Carbon* 49 (2011) 5298–5311.
- [26] C. Russo, A. D'Anna, A. Ciajolo, M. Sirignano, *Combust. Flame* 167 (2016) 268–273.
- [27] M. Sirignano, D. Bartos, M. Conturso, M. Dunn, A. D'Anna, A.R. Masri, *Combust. Flame* 176 (2017) 299–308.
- [28] K. Hayashida, S. Nagaoka, H. Ishitani, *Fuel* 128 (2014) 148–154.
- [29] K. Hayashida, Y. Miki, *Bunseki Kagaku* 66 (2017) 343–350.
- [30] C.K. Law, *Combustion Physics*, Cambridge Press, Cambridge, 2006.
- [31] R.A. Dobbins, G.J. Govatzidakis, W. Lu, A.F. Schwartzman, R.A. Fletcher, *Combust. Sci. Technol.* 121 (1996) 103–121.
- [32] M.R. Khalghy, A. Veshkini, M.J. Thomson, *Carbon* 100 (2016) 508–536.
- [33] A. Veshkini, S.B. Dworkin, M.J. Thomson, *Combust. Flame* 161 (2014) 3191–3200.
- [34] T.S. Totton, D. Chakrabarti, A.J. Misquitta, M. Sander, D.J. Wales, M. Kraft, *Combust. Flame* 157 (2010) 909–914.
- [35] C. Saggese, S. Ferrario, J. Camacho, et al., *Combust. Flame* 162 (2015) 3356–3369.
- [36] G. Blanquart, H. Pitsch, *Combust. Flame* 156 (2009) 1614–1626.
- [37] A.D. Abid, N. Heinz, E.D. Tolmachoff, D.J. Phares, C.S. Campbell, H. Wang, *Combust. Flame* 154 (2008) 775–788.
- [38] M. Sirignano, A. D'Anna, *Proc. Combust. Inst.* 34 (2013) 1877–1884.
- [39] C. Gu, H. Lin, J. Camacho, et al., *Combust. Flame* 165 (2016) 177–187.
- [40] M.M. Maricq, *Combust. Flame* 144 (2006) 730–743.
- [41] C.A. Echavarria, A.F. Sarofim, J.S. Lighty, A. D'Anna, *Combust. Flame* 158 (2011) 98–104.
- [42] A.D. Abid, J. Camacho, D.A. Sheen, H. Wang, *Energy Fuels* 23 (2009) 4286–4294.
- [43] J. Camacho, S. Lieb, H. Wang, *Proc. Combust. Inst.* 34 (2013) 1853–1860.
- [44] K.V. Puduppakkam, A.U. Modak, C.V. Naik, J. Camacho, H. Wang, E. Meeks, *AMSE Turbo Expo*, 2014 V04BT04A055-C051.
- [45] H. Lin, C. Gu, J. Camacho, et al., *Combust. Flame* 172 (2016) 365–373.
- [46] Q. Tang, B. Ge, Q. Ni, B. Nie, X. You, *Combust. Flame* 187 (2018) 239–246.
- [47] L.A. Sgro, A. De Filippo, G. Lanzuolo, A. D'Alessio, *Proc. Combust. Inst.* 31 (2007) 631–638.
- [48] P. Minutolo, A. D'Anna, A. D'Alessio, *Combust. Flame* 152 (2008) 287–292.
- [49] Q. Tang, R. Cai, X. You, J. Jiang, *Proc. Combust. Inst.* 36 (2017) 993–1000.
- [50] J. Camacho, A.V. Singh, W. Wang, et al., *Proc. Combust. Inst.* 36 (2017) 1001–1009.
- [51] A.D. Abid, J. Camacho, D.A. Sheen, H. Wang, *Combust. Flame* 156 (2009) 1862–1870.
- [52] J. Camacho, C. Liu, C. Gu, et al., *Combust. Flame* 162 (2015) 3810–3822.
- [53] C. Saggese, A. Cuoci, A. Frassoldati, et al., *Combust. Flame* 167 (2016) 184–197.
- [54] F. Carbone, M. Attou, A. Gomez, *Aerosol Sci. Technol.* 50 (2016) 740–757.
- [55] F. Carbone, S. Moslih, A. Gomez, *Combust. Flame* 181 (2017) 329–341.
- [56] Z. Li, H. Wang, *Phys. Rev. E* 68 (2003) 061207.
- [57] H. Guo, J.A. Castillo, P.B. Sunderland, *Appl. Opt.* 52 (2013) 8040–8047.
- [58] R.J. Kee, J.A. Miller, G.H. Evans, G. Dixon-Lewis, *Proc. Combust. Inst.* 22 (1989) 1479–1494.
- [59] H. Wang, X. You, A.V. Joshi, et al., *USC Mech II: High-Temperature Combustion Reaction Model of H₂/CO/Cl-C4 Compounds* (2007) http://ignis.usc.edu/USC_Mech_II.htm.
- [60] R.P. Lindstedt, B.B.O. Waldheim, *Proc. Combust. Inst.* 34 (2013) 1861–1868.
- [61] E.K.Y. Yapp, D. Chen, J. Akroyd, et al., *Combust. Flame* 162 (2015) 2569–2581.
- [62] M. Lucchesi, A. Abdelgadir, A. Attili, F. Bisetti, *Combust. Flame* 178 (2017) 35–45.
- [63] G.A. Kelesidis, E. Goudeli, S.E. Pratsinis, *Proc. Combust. Inst.* 36 (2017) 29–50.
- [64] F. Tuinstra, J.L. Koenig, *J. Chem. Phys.* 53 (1970) 1126–1130.
- [65] P. Lespade, R. Al-Jishi, M.S. Dresselhaus, *Carbon* 20 (1982) 427–431.
- [66] M.A. Pimenta, G. Dresselhaus, M.S. Dresselhaus, L.G. Cancado, A. Jorio, R. Saito, *PCCP* 9 (2007) 1276–1290.
- [67] A.C. Ferrari, J. Robertson, *Phys. Rev. B* 61 (2000) 14095–14107.
- [68] A.C. Ferrari, D.M. Basko, *Nat. Nanotechnol.* 8 (2013) 235.
- [69] P. Mallet-Ladeira, P. Puech, C. Toulouse, et al., *Carbon* 80 (2014) 629.